Journal of Medical Systems (2019) 43: 289
https://doi.org/10.1007/s10916-019-1413-3

IMAGE & SIGNAL PROCESSING

Region Extraction and Classification of Skin Cancer: A Heterogeneous framework of Deep CNN Features Fusion and Reduction

Tanzila Saba[1] · Muhammad Attique Khan[2] · Amjad Rehman[3] · Souad Larabi Marie-Sainte[1]

Received: 5 March 2019 / Accepted: 3 July 2019 / Published online: 20 July 2019

Abstract

Cancer is one of the leading causes of deaths in the last two decades. It is either diagnosed malignant or benign – depending upon the severity of the infection and the current stage. The conventional methods require a detailed physical inspection by an expert dermatologist, which is time-consuming and imprecise. Therefore, several computer vision methods are introduced lately, which are cost-effective and somewhat accurate. In this work, we propose a new automated approach for skin lesion detection and recognition using a deep convolutional neural network (DCNN). The proposed cascaded design incorporates three fundamental steps including; a) contrast enhancement through fast local Laplacian filtering (FlLpF) along HSV color transformation; b) lesion boundary extraction using color CNN approach by following XOR operation; c) in-depth features extraction by applying transfer learning using Inception V3 model prior to feature fusion using hamming distance (HD) approach. An entropy controlled feature selection method is also introduced for the selection of the most discriminant features. The proposed method is tested on PH2 and ISIC 2017 datasets, whereas the recognition phase is validated on PH2, ISBI 2016, and ISBI 2017 datasets. From the results, it is concluded that the proposed method outperforms several existing methods and attained accuracy 98.4% on PH2 dataset, 95.1% on ISBI dataset and 94.8% on ISBI 2017 dataset.

Keywords Skin cancer · Augmentation · Contrast improvement · Boundary extraction · Deep learning · Features selection

Introduction

The studies of the World Health Organization (WHO) assess that skin cancer has a share of one-third of all diagnosed cancers cases and the incidence rate continues to rise worldwide. The factors of increase rest in ozone layer reduction which is responsible for the protection against ultraviolet radiations. Skin cancer has two types: melanoma and non-melanoma. More than 87,000 melanomas and over five million non-melanoma cases are diagnosed each year only in the US [1]. Melanoma is the most dangerous type of skin cancer and begins in pigment cells. Approximately 75% of deaths related to skin cancer occurred due to malignant lesions [2]. Doctors in the clinics use some advanced and sophisticated treatment methods and tools, such as immunotherapy and radiation therapy along with surgery clinical tools. The five-year survival ratio of advanced stage cases is still below than 15%, whereas the survival rate for early-stage cases is over 95% [3]. This difference identifies that the patient survival rate highly depends on the timely detection and treatment of melanoma. Therefore, the primary goal is to diagnose melanoma in its early stages [4, 5].

In order to improve the melanoma diagnostic accuracy, most of the dermatologists used a popular noninvasive imaging method known as dermoscopy. In dermoscopy, first, a gel is placed on the lesion area. Later, by using a

Highlights
- This research presents a novel approach for microscopic skin lesion boundary extraction and lesion recognition through Deep Neural Network.
- Distinction features are selected through clustering controlled entropy approach and classified through MLP.

This article is part of the Topical Collection on *Image & Signal Processing*

✉ Amjad Rehman
rkamjad@gmail.com

Tanzila Saba
drtsaba@gmail.com

[1] College of Computer and Information Sciences, Prince Sultan University, Riyadh 11586, Saudi Arabia

[2] Department of Computer Science and Engineering, HITEC Universit, Museum Road, Taxila, Pakistan

[3] College of Computer and Information Sciences, Imam Mohammad Ibn Saud Islamic University, Riyadh, Saudi Arabia

magnifier tool, an illuminated and magnified image acquires which provides better visualization of the pigment structure of the lesion [6]. It improves the diagnostic rate significantly compared to the examination with a naked eye. Moreover, it has been showed that dermoscopy has a detection accuracy reaching approximately 75% [7]. The doctors used a few well-known diagnostics tools in the clinics such as ABCDE rule, seven-point checklist, optical techniques such as laser and few more. However, the manual interpretation of dermoscopic images is time-consuming and subject of dermatologist experience and clinical training. Besides, an experienced dermatologist may produce an error during the diagnostic process [8]. Therefore, a computerized based diagnostic and analysis methods are required will assist the dermatologist for fast detection and to improve the detection accuracy. The researchers' community from the field of image processing and machine learning (ML) put great efforts in the development of automated based melanoma diagnostic tools referred to as computer-aided diagnosis (CAD) systems. These methods overcome the issues of traditional dermoscopy techniques [9].

The performance of ML in the area of medical image analysis has shown significant outputs in the detection, diagnosis, and analysis of medical objects [10–13]. For example, skin lesions are complex and difficult to predict precisely while using a simple design [14]. Through these ML designs, the objects like lesions are categorized into their relevant classes such as melanoma, basal cell carcinoma, and benign. These models are based on the feature based ML design which is harder for a massive number of images dataset [15]. Lately, the emergence of deep learning in the area of ML has given a higher performance in medical imaging. The DL based on the classification process is also known as image-based ML because the images are directly put to the DL design as input. The deep learning methods are highly useful when the number of training inputs is large [16].

Problem statement and contributions

The computerized based melanoma detection and recognition is still a very challenging task. Few of major general issues are similar colors of healthy and skin lesions, change in lesion shapes, texture, change among normal and skin lesion, and presence of a lesion on the boundary areas. Some other artifacts such as illumination, veins, hairs, air bubbles, color calibration marks, and many more affect the segmentation and reduce the feature extraction accuracy [17]. By using deep learning, the researchers mostly faced the problems of irrelevant features which reduce the recognition accuracy of the designed DL model. In this work, we design a new heterogeneous model for skin lesion detection and classification through enhancing color convolutional network (ECCN) and fusion of fully connected and average pool layers of inception v3 Deep CNN model. Our major contributions are:

1) In the preprocessing phase, an augmentation is performed in the initial step for an equal length of all classes of cancer types. Then, enhancing the images through fast local Laplacian filtering (FlLpF) along with HSV color transformation defined by (FlLpFaHSV) for the next process.
2) The enhanced HSV transformed data is utilized for the segmentation process, in which the color labels are assigned (Pink and Yellow). The yellow color depicts healthy pixels, whereas the Pink color describes lesion pixels. Through color labels, the sample is split into 60% for training the deep CNN model and 40% for testing the segmentation effects. Additionally, the thresholding and morphological operations are utilized for the retrieval of a binary image.
3) The deep CNN features are extracted through FC and AP layers of Inception V3 pre-trained model, then the features are mapped to the selected dermoscopy dataset through fine-tuning. The extracted FC and AP layer features are fused through Hamming distance.
4) The fused CNN features are divided into two clusters based on the mean threshold value and the computed entropy value. Then, the posterior probability values are computed for each cluster. After that, the initial probability values are updated until the error rate is close to zero. This process almost reduces the features number by 60%. Finally, concatenate both cluster features after clustering controlled entropy (CcE) is performed and then apply one of the famous classification methods such as SVM, K-Nearest Neighbor, and neural network (NN).

The rest of the paper is organized into four main sections. Section "Related work" presents the recent state of the art. Section "Proposed methodology" exhibits the proposed methodology. Section "Experimental results and discussion" addresses the results and discussion. Finally, section "Conclusion" concludes the research.

Related work

In the last two decades, different computer-based systems have been developed to solve the challenges related to melanoma segmentation and recognition. Four primary steps are performed in any computerized method such as i) preprocessing, ii) lesion boundary detection, iii) feature extraction and selection, and iv) classification. The

preprocessing step is performed to increase the quality of images and removes some artifacts like hairs, air bubbles, illumination, and poor contrast which may complicate the next step. As a matter of fact it is the main requirement. Many approaches have been utilized for removing these challenges such as software-based hair removal, morphological operation bases removal, filtering, contrast stretching, masking, and few more. Lee et al. [18] presented a software-based hair removal method referred to as DullRazor using morphological operations. Kiani et al. [19] improves the DullRazor method and make it capable of removing both thick and light hairs from dermoscopic images. [20] proposed a method for illumination correction from lesion images by using polynomial curve fitting and bilateral decomposition. Most recently, Nasir et al. [4, 5] utilized texture and color information of lesion for contrast enhancement. Lesion Segmentation is the second most important step for lesion segmentation. The prosperity of these analysis systems is highly dependent on the reliability and robustness of the segmentation step. It is complicated to develop an accurate and efficient segmentation algorithm by considering different sizes, shapes, color, and texture of lesions as well as different types of skins. To conquer these problems, different approaches are used in theliterature. These approaches are based on region which use region growing techniques [21], clustering methods which differentiate the lesion pixels from healthy skin pixels and homogeneous areas [22], thresholding techniques [22], and active contours approaches which iteratively detect the lesion border [23].

Feature extraction step is involved in the extraction of essential features which correctly describe the current problem. After that, the selection of efficient one is required for reducing the computational complexity and increase the overall system accuracy. Color, shape, and texture features are the most widely used features for lesion detection [24]. Sadeghi et al. [25] explain the importance of irregular patterns in the lesion for diagnosis process. However, these features do not perform well for a large number of training samples. These irregular patterns include color and texture features. Satheesha et al. [26] extract shape (2D, 3D), texture, and color features of the lesion and select the most appropriate features by using heuristic approach. The importance of color features in the classification process is presented in [27]. A clustering based method is used to extract color features. Moreover, automated segmentation of skin lesions through CNN has given a significant performance compared to recent well-known techniques like thresholding, etc. Philip et al. [28] described an encoder weighted based approach for lesion segmentation. They utilized ResNet-34 approach along with ISIC2017 dataset. Mahbod et al. [29] designed an ensemble CNN approach for skin lesion segmentation. In the developed approach, intra and inter architectures are merged for features abstraction levels and each architecture consists of multiple pre-trained CNN networks and fine-tuned on given dermoscopy images. Finally, the extracted features through fine-tuning are fed to SVM for classification. The experiments are performed on ISIC2017. The obtained results outperformed the top-ranked techniques. Pedro et al. [30] extracted structural co-occurrences matrices (SCM) for textural features extraction from dermoscopic images. These extracted features have powerful discrimination compared to other textural features. The evaluation is performed on ISIC 2016 and 2017 datasets and reached a specificity of more than 90%. The extracted features are mostly classified through supervised learning algorithms based on their pros and cons. SVM classifier is the most commonly used in computerized lesion classification. Other widely used classifiers in the literature include decision trees, k-nearest neighbor, artificial neural networks (ANN), and linear discriminate analysis (LDA) [31, 32].

Proposed methodology

The proposed lesion segmentation and recognition system are based on the contrast-enhanced deep CNN design which comprises three primary steps: (a) data augmentation and contrast-enhanced for lesion visibility, (b) color value based lesion identification and lesion boundary extraction, and (c) DCNN features extraction, fusion, and selection for recognition. Flow architecture of the proposed system is shown in Fig. 1.

Dataset augmentation & contrast enhancement

In medical imaging, the problem of imbalance classes affects the accuracy of the system. Therefore, it is essential to resolve the imbalance issue through the rotation, filtering, and a few other techniques [33]. Nowadays, in medical imaging, skin cancer is a very hot topic in research, but the availability of datasets in this area is a challenge for researchers. The available datasets include a vast difference between the number of images in each class. For example, PH2 dataset includes a total of 200 images divided into40images in melanoma class, 80images in common nevi class, and 80 images in atypical nevi class. The melanoma class has half the number of images containing in the other two classes which causes degradation of the recognition accuracy. In this work, we rotate the images into 4 different angles (45^0, 60^0, 135^0, 270^0) for the principle of data augmentation. This process is performed only in the training phase.

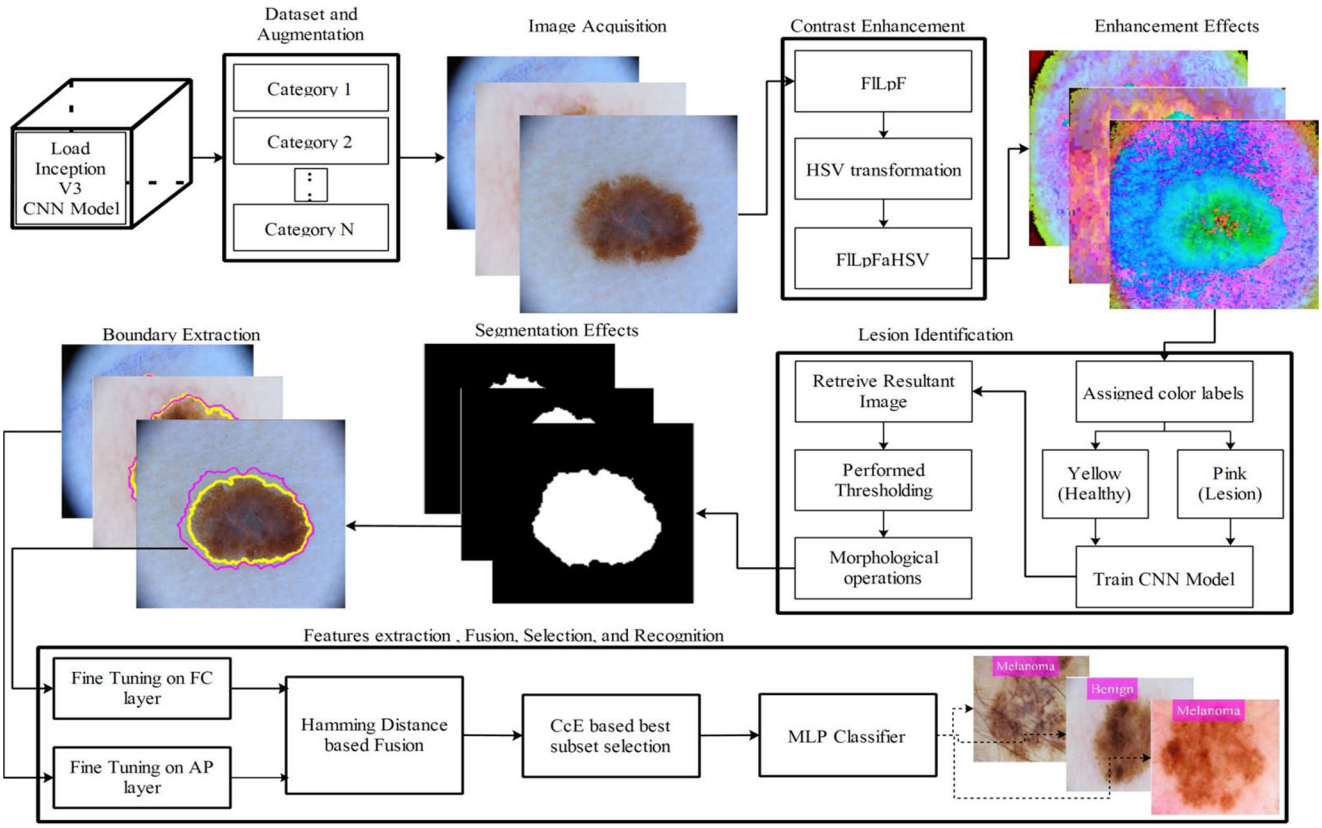

Fig. 1 Proposed workflow of stomach infection segmentation and recognition

Following, the augmentation step, color enhancement is performed through the fast local Laplacian filtering (FlLpF) along with the HSV color transformation. This approach processes through two steps. Initially, the

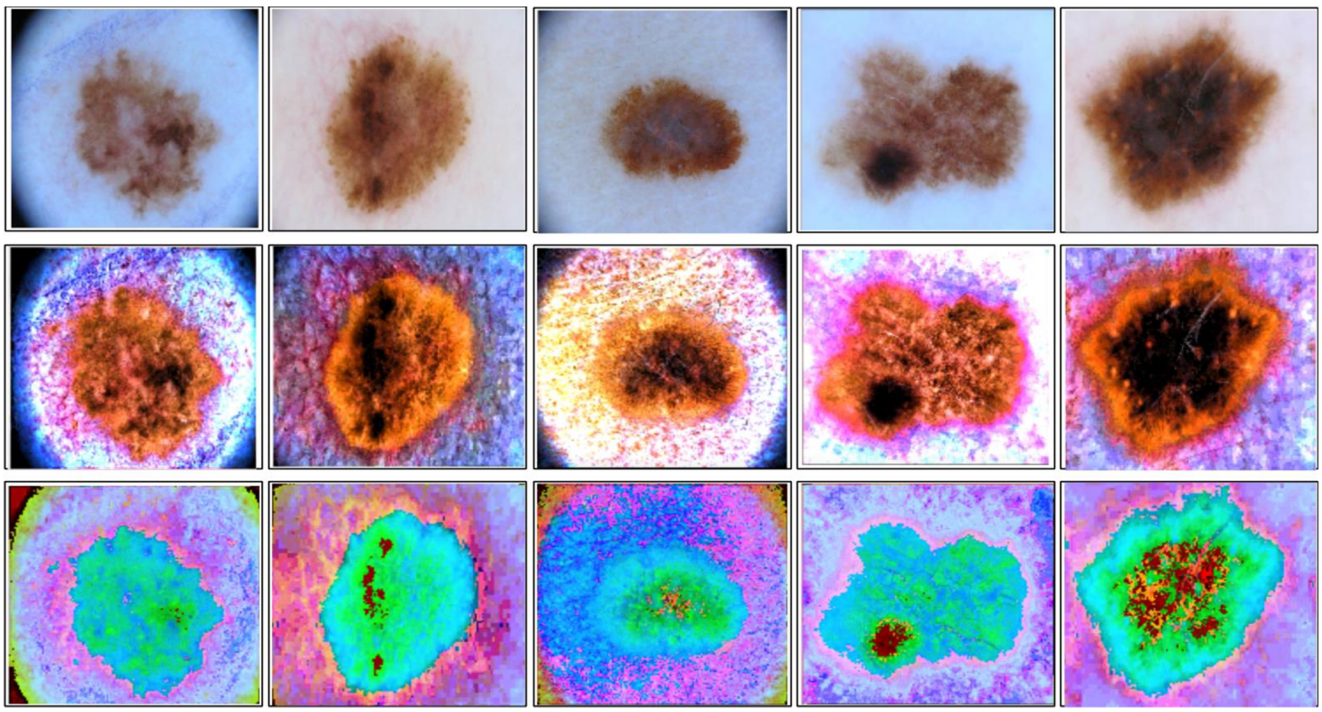

Fig. 2 Proposed FlLpFaHSV enhancement effects. The first row represents original images, second row shows the FILpF effects, and bottom row demonstrate the effects after HSV transformation

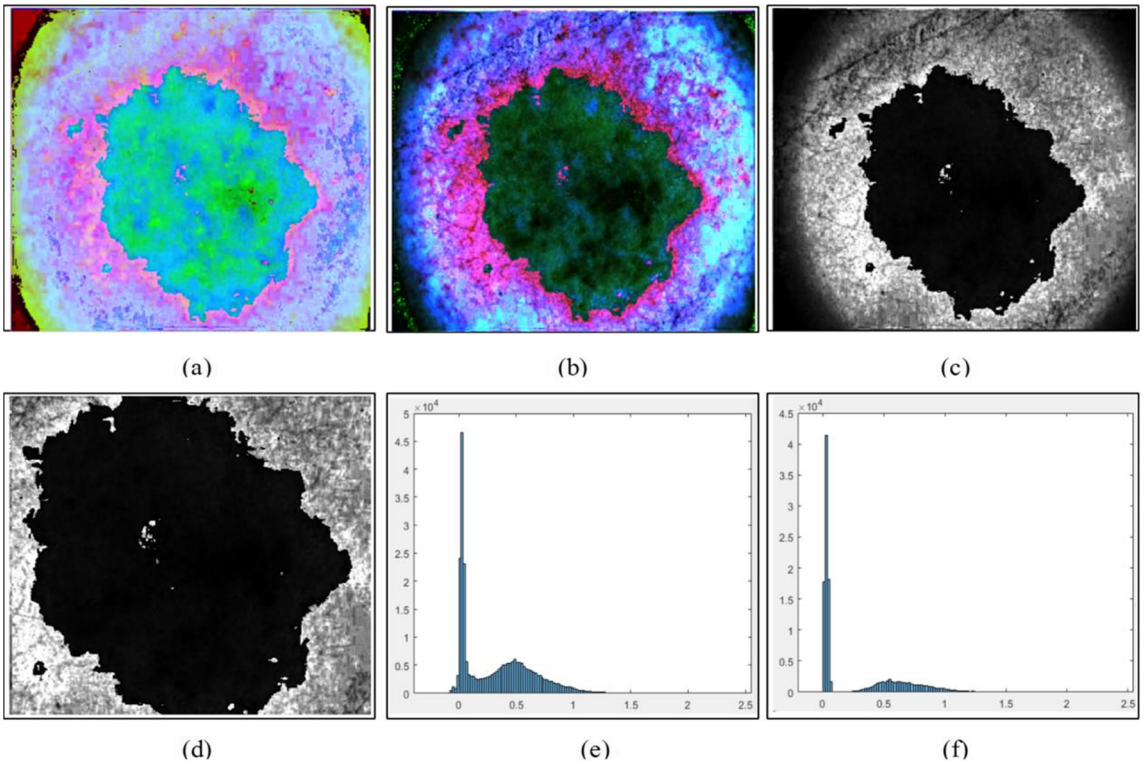

Fig. 3 XOR operation effects on sample images. **a** Enhanced image, **b** XOR operation, **c** selection of first channel after XOR operation, **d** selection of lesion part for identifying their pixels, **e** histogram of first channel of XOR image, and **f** selection range of 110-460 for lesion pixels

FlLpF approach is implemented through the following formulation:

Let have the input image I of dimensions 512×512 at position(x, y). Let φ denotes the results output image of dimension 512×512 at position(x, y). Let $\{\xi_L[\varphi_{x,\ y}]\}$ denotes the laplacian pyramid (LP) which constructs coefficients, where each constructed coefficient is independent to other coefficients. At the initial stage, the simple pixel wise filtering is performed on the original image$I$, then compute LP through a transformed image. Through

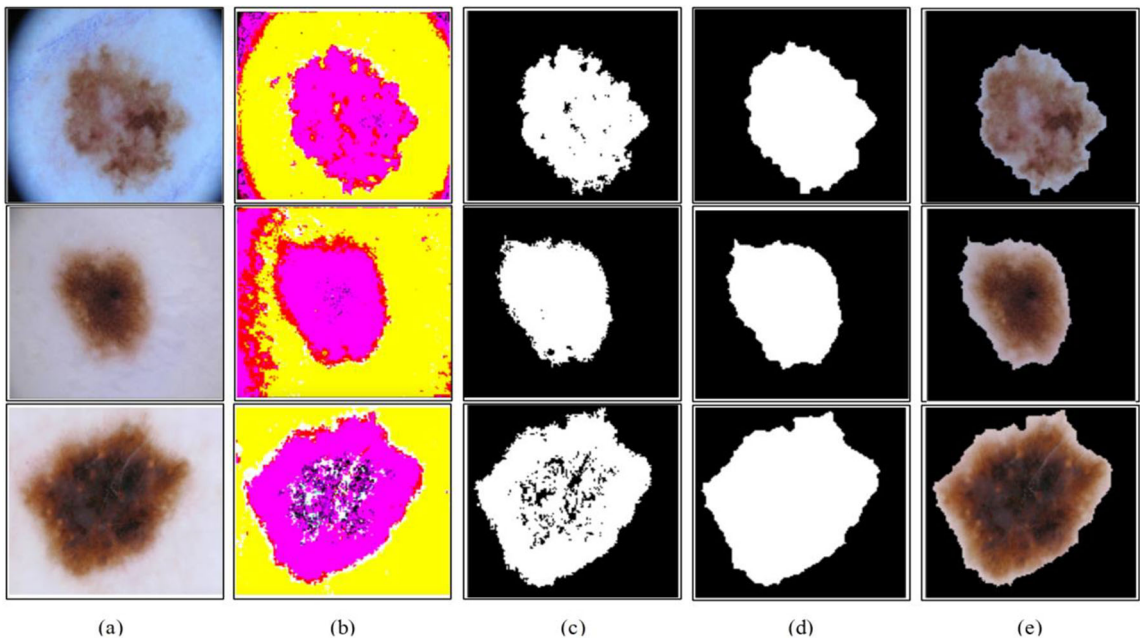

Fig. 4 Proposed segmentation effects through previous pixels color information. **a** Original image, **b** CNN labeled image, **c** thresholding, **d** refinement, and **e** mapped RGB

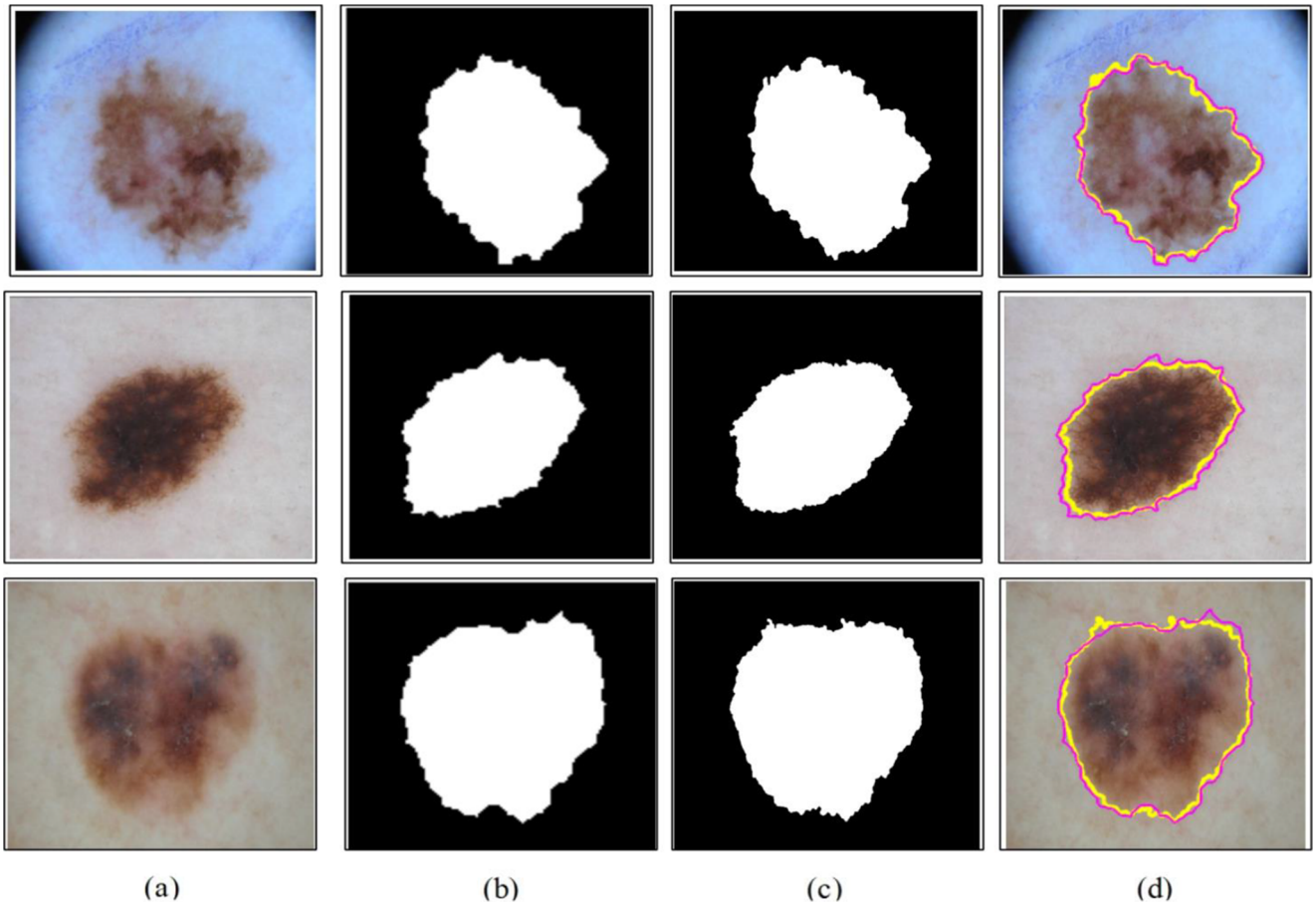

Fig. 5 Proposed boundary extraction effects. **a** Original image, **b** proposed segmented, **c** ground truth, and **d** boundary detection

LP, the laplacian coefficient $\xi_L^l[\varphi_{x,\ y}]$is computed at level l and position(x, y). This process is repeated for all coefficients [34].

After computing the resultant $\xi_L^l[\varphi_{x,\ y}]$image, the HSV transformation is applied. Through HSV transformation, the highlighted edges of the lesion parts are further improved. The mathematical formulation of HSV is represented by ξ_{HSV} andthe formulation is done through Eq. (1-3).

$$\xi_H = 60^0 \times \xi_{H'} \tag{1}$$

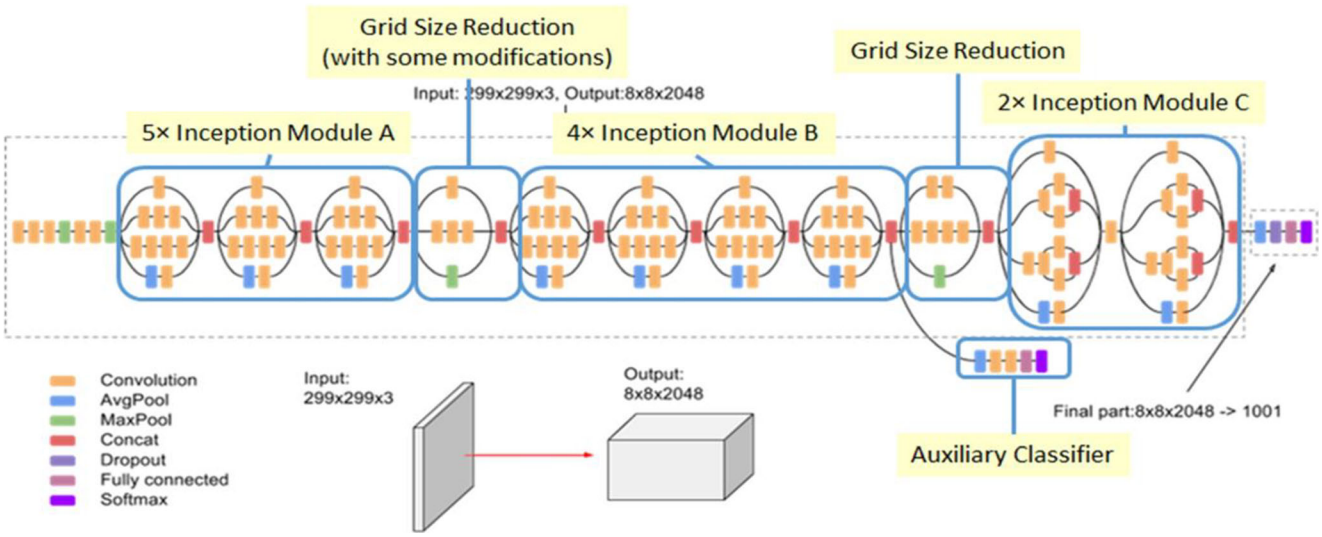

Fig. 6 Architecture of Inception V3 framework

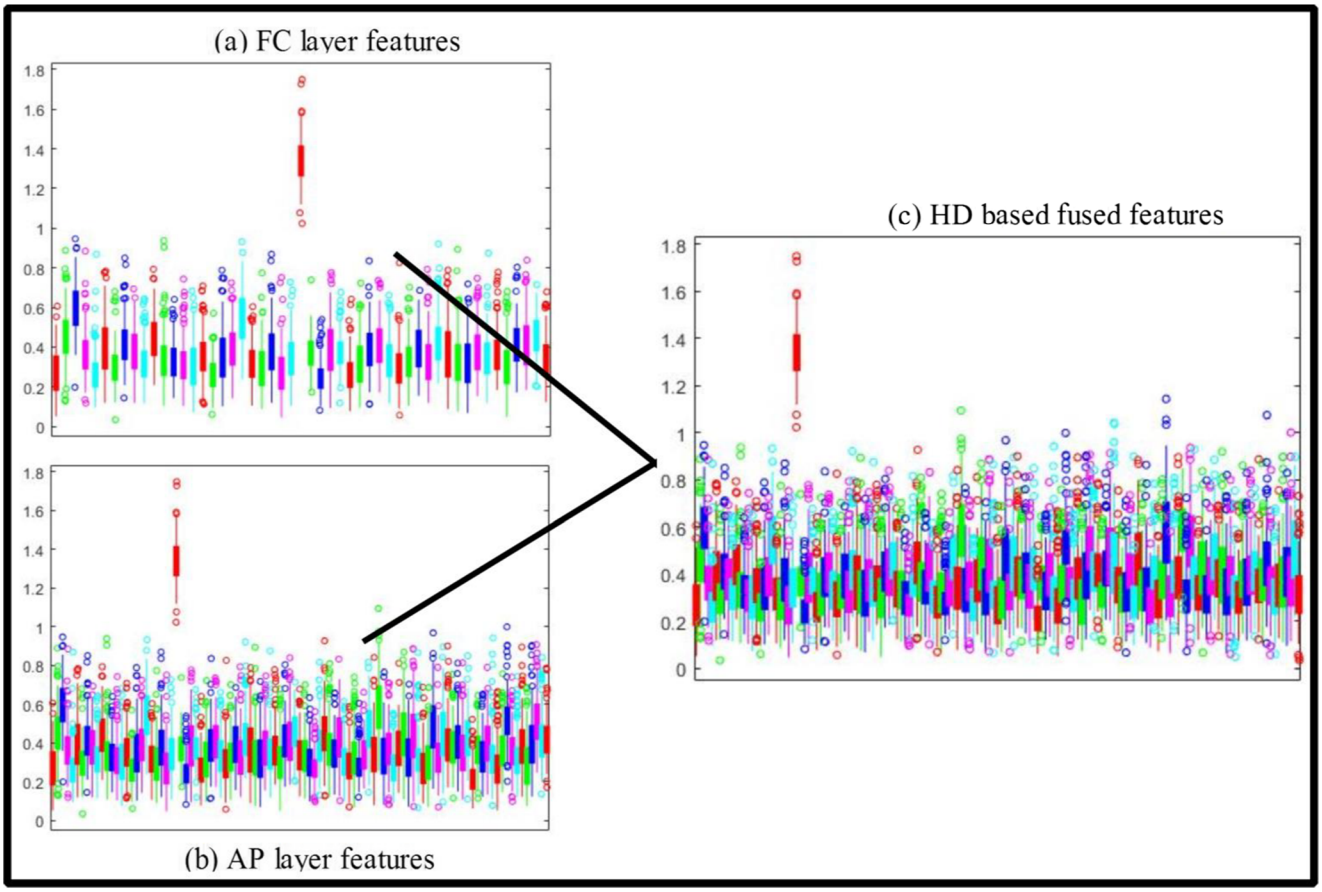

Fig. 7 Proposed HD based fusion representation

$$\xi_{H'} = \begin{cases} \frac{\xi_G - \xi_B}{C} & if\ M = \xi_R \\ \frac{\xi_G - \xi_B}{C} + 2 & if\ M = \xi_G \\ \frac{\xi_G - \xi_B}{C} + 4 & if\ M = \xi_B \end{cases} \quad (2)$$

$$\xi_S = \begin{cases} 0 & \xi_V = 0 \\ \frac{C}{\xi_V} & Otherwise \end{cases} \quad (3)$$

Where, $V = M$, $M = \max(\xi_R, \xi_G, \xi_B)$, C is a constant value which is defined through the difference of the maximum and the minimum image pixels information as $C = M - m$, and $m = \min(\xi_R, \xi_G, \xi_B)$. The$\xi_R$, ξ_G, and ξ_B represent the red, green, and blue channels of the transformed image ${\xi_L}^l[\varphi_{x,\ y}]$. The sample resultant images are shown in Fig. 2, which are later utilized for lesion identification.

Boundary extraction

The boundary extraction of skin lesion is an essential and challenging task in the area of computer vision. In general, the boundary extraction phase consists of two steps including lesion segmentation and identification. Before performing the boundary extraction, it is essential to find out the lesion from the input image. In the literature, various types of techniques are introduced for lesion segmentation and boundary extraction. The most famous methods are thresholding based lesion extraction [35], region growing based lesion segmentation [36], CNN based segmentation [37], and few more [38, 39]. From all, the deep learning based segmentation techniques are well accurate in terms of automation and efficiency.

In this work, we proposed a new deep neural network (DCNN) approach for skin lesion segmentation and later identification. In the proposed approach, initially, we divide the dataset into training and testing. Both training and testing samples include both original and their ground truth images. The stepwise formulation of this process is defined as follows:

Let, T_1 denotes training and testing images set, T_2 denotes their corresponding labels set, then before further processing, we perform XOR operation on the enhanced image ξ_{HSV} and FlLpF image ${\xi_L}^l$ for range selection of lesion pixels. The XOR operation is defined as:

$${\xi_L}^l(i) \cup \_ \xi_{HSV}(j) = \left({\xi_L}^l(i) \cap !\xi_{HSV}\left(j\right) \cup \left(!{\xi_L}^l(i) \cap \xi_{HSV}(j)\right)\right) \quad (4)$$

$$= \left(\xi_L^l(i) \cup \xi_{HSV}(j)\right) \cap \left(!\xi_L^l(i) \cap !\xi_{HSV}(j)\right) \quad (5)$$

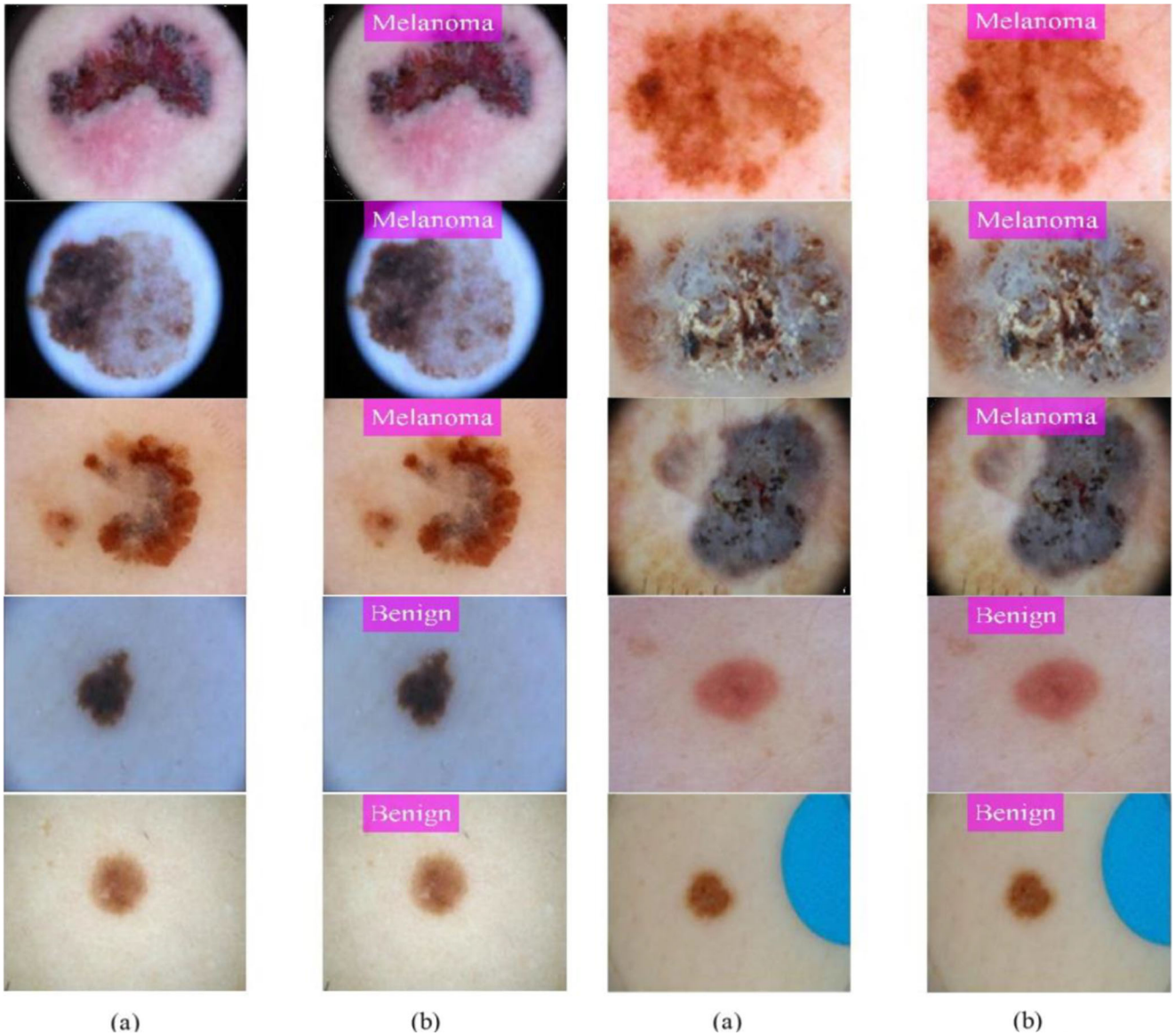

Fig. 8 Proposed labeled results. **a** Original dermoscopy image, **b** proposed labeled image

Where ∪ denotes union operation, ∩ denotes intersection operation, and ! explains not operation. The effects of XOR operation are shown in Fig. 3. In Fig. 3c, the first channel of XOR image is extracted and later select the most nearly lesion pixel points. The probability is computed to find out the exact lesion pixel values that later utilized for training the CNN model. Through the probability value, it is clearly showed that the pixels in range of 0-0.4 are best representing the lesion pixels, while pixels greater than this range represent background or healthy regions, as shown in Fig. 3f. The maximum pixel value is selected 0.4 using trial and error method.

These lesion and healthy pixels are defined into two separate classes denoted by $\Delta_1$and Δ_2, respectively. Then, load VGG19 pre-trained CNN model. Through fine-tuning, train the model using lesion and healthy region pixel values. The few of essential parameters are also defined like padding mode is manual, pooling size is 2 × 2, a number of max epochs are 200, Min Batch Size is 64, and the learning rate is 0.2. After that, the activation is performed through the following loss function:

$$F_{\xi} = -\frac{1}{N_i \times M_j}\sum_{i,j} \left[y_{i,j} \ln p\left(w|\xi_{i,j}\right) + \left(1-y_{i,j}\right)\ln\left(1-p\left(w|\xi_{i,j}\right)\right)\right] \quad (6)$$

Where, $y_{i,\ j}$ denotes class labels $((y_{i,\ j}) \in \{pink, yellow\})$ and $\xi_{i,\ j}$ are actual pixels of the image. After performing this activation function, anOtsu threshold operation is performed and later refined through morphological operations such as closing, filling, and area removal [40] as shown in Fig. 4.

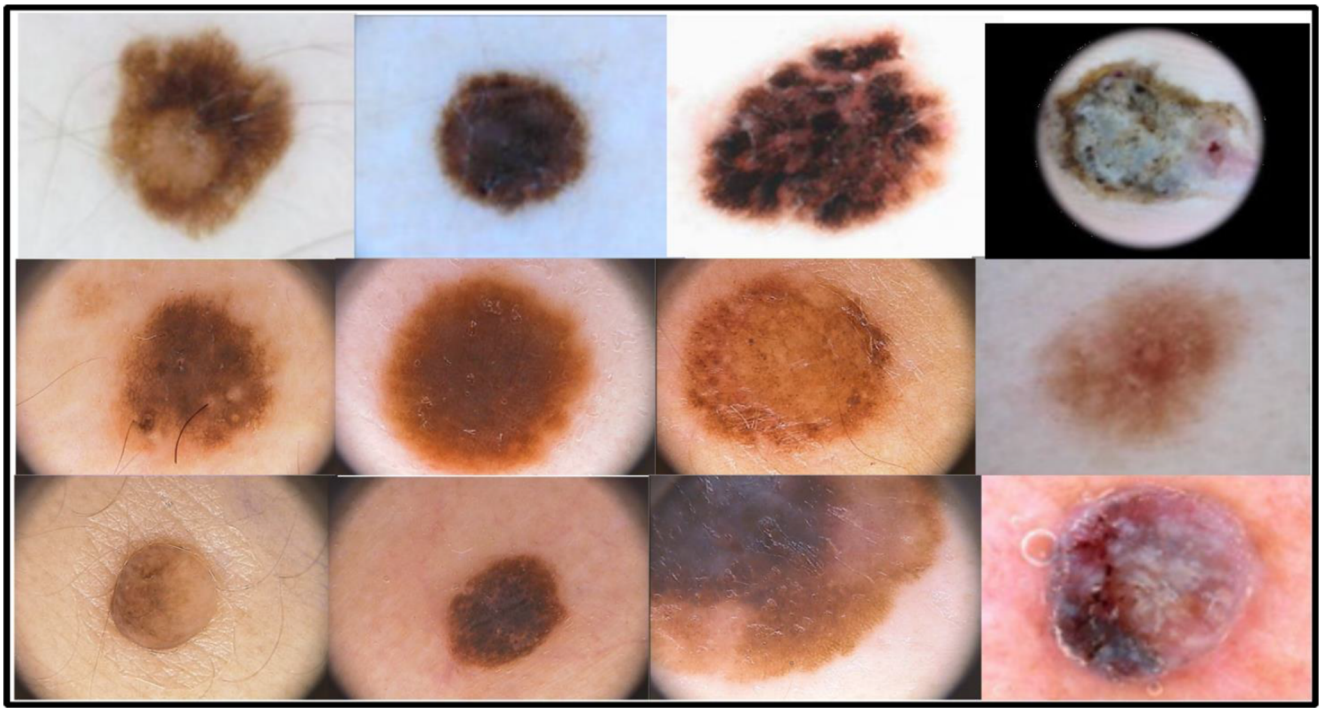

Fig. 9 Samples dermoscopy images

Moreover, the boundary extraction is done through the comparison of the proposed segmented and the ground truth image, as shown in Fig. 5. The comparison among the ground truth image and the proposed segmented image is defined through Eq. (7).

$$\xi_{bd}(i,j) = 1 - \frac{|\xi_{GR}(i) \cap \xi_{RG}(j)|}{|\xi_{GR}(i)| + |\xi_{RG}(j)| - |\xi_{GR}(i) \cap \xi_{RG}(j)|} \quad (7)$$

Where, $\xi_{GR}(i)$ denotes the ground truth image pixels and $\xi_{RG}(j)$ denotes the proposed refined segmented image.

DCNN features and recognition

In the area of machine learning (ML), the performance of a system is dependent on the extraction of most strong kind features [41–45]. In medical imaging, mostly color, texture, and shape features are used for the classification

Table 1 Segmentation accuracy for ISIC 2017 dataset using testing data; (* denotes the overall segmentation accuracy of all training images)

Image No	Accuracy (%)	Negative rate (%)	Image No	Accuracy (%)	Negative rate (%)
1	98.25	1.75	16	88.47	11.53
2	96.56	3.44	17	88.91	11.09
3	96.12	3.88	18	89.17	10.83
4	94.27	5.73	19	89.92	10.08
5	95.95	4.05	20	90.62	9.38
6	95.89	4.11	21	92.91	7.09
7	95.14	4.86	22	92.98	7.02
8	97.94	2.06	23	91.67	8.33
9	97.61	2.39	24	91.88	8.12
10	97.29	2.71	25	93.79	6.21
11	96.80	3.2	26	92.35	7.65
12	96.42	3.58	27	91.51	8.49
13	96.91	3.09	28	94.34	5.66
14	96.97	3.03	29	94.66	5.34
15	96.56	3.44	30	94.80	5.2
*Overall Average				94.78	5.22

Table 2 Segmentation accuracy for PH2 dataset using testing data; (* denotes the overall segmentation accuracy of all training images)

Image No	Accuracy (%)	Negative rate (%)	Image No	Accuracy (%)	Negative rate (%)
1	98.11	1.89	11	94.01	5.99
2	98.19	1.81	12	94.19	5.81
3	98.71	1.29	13	94.89	5.11
4	98.75	1.25	14	94.99	5.01
5	98.80	1.2	15	97.56	2.44
6	98.88	1.12	16	97.11	2.89
7	96.59	3.41	17	97.89	2.11
8	96.41	3.59	18	97.90	2.1
9	96.11	3.89	19	97.95	2.05
10	94.12	5.88	20	97.98	2.02
*Overall Average				95.41	4.59

process [46–50], but these techniques do not perform well when the processed data is vast in number. Researchers resolve this kind of problem through deep learning in the area of ML [46, 51–53]. In this work, we utilized a pre-trained inception V3 DCNN model based on its high speed and best accuracy. The original architecture of Inception V3 is shown in Fig. 6 [54].

Inception V3 CNN pre-trained model is introduced after the modification of GoogleNet architecture. The base of this model is replaced by 3 × 3 convolutions whereas the previous GoogleNet has 5 × 5 convolutions. The resultant network includes ten inception modules. The modules of GoogleNet are changed by substituting the nxn convolutions by 1 × 7 followed by a 1 × 1 which reduced the computational time. The last two modules of GoogleNet are replaced by 1 × 3 and 3 × 1 in parallel. Lastly, the original 7 × 7 convolutions of GoogleNet model are modified by 3 × 3 convolutions. Hence, in total 42 learnable layers are included in Inception v3 CNN model.

Features are extracted through performing the activation on FC and AP layers of Inception V3 model in parallel through fine-tuning. This process includes two-step as training and testing. In the training phase, the input dataset is divided into a 70:30 which explains that 70% of samples are utilized for training the model and the remaining 30% for testing the proposed system. The dimensions of the features extracted through FC and AP layers are Nx1000 and Nx20148 respectively. Later, the extracted features from both layers are fused through the Hamming Distance (HD) approach as described below.

Table 3 Comparison of proposed segmentation accuracy for ISIC 2017 and PH2 dataset

Method	Dataset	Year	Accuracy (%)
[56]	ISIC 2017	2019	94.08
[59]	ISIC 2017	2018	85.40
[60]	ISIC 2017	2018	83.90
[61]	ISIC 2017	2019	93.80
[62]	ISIC 2017	2017	91.00
[56]	PH2	2019	95.30
[63]	PH2	2017	94.24
Proposed	ISIC 2017	2019	94.78
Proposed	PH2	2019	95.41

Let X denotes the number of the extracted features represented as $Fc_l$and AP_l. Let the values of the extracted features are $\Delta = \{x_1, x_2, \ldots x_n - 1\}$. Then Δ is representable according to a bijection f: $\{c_i, c_j\} \leftrightarrow \Delta$. We defined the distortion $D(f, c_i, c_j)$ under the bijection$f$ between two feature sets $c_i, c_j \in \{R\}^n$ as the normalized D_1,the distance of their corresponding features.

$$D(f, c_i, c_j) = \frac{|f(c_i) - f(c_j)|}{2^X} \tag{8}$$

Where, c_i, $c_j \in \{R\}^n$ and R represent the real values of the extracted features. Let $D_H(x_i, x_j)$ be the HD between two feature sets $c_i$and c_j, then the maximum distance between two feature sets is assumed as follows:

$$D_H{}^{(max,1)}(f, c) = \max_{\{c: D_H(c,x)=1\}} D(f, c, x) \tag{9}$$

Then, the distance-1 distortion is defined under bijection f as:

$$D_H{}^{(max,1)}(f) = \max_{c \in \{R\}^n} D_H{}^{(max,1)}(f, c) \tag{10}$$

Where, $D_H{}^{(max,1)}$ defines the max distance features that replaces the lower distance value feature at fusion place. The size of the fused vector is $N \times 2048$ denoted by δF which later is selected through anew implemented clustering controlled entropy (CcE) approach. The visual representation of the fusion process is shown in Fig. 7.

Table 4 Proposed recognition results through HD based features fusion and CcE selection approach using PH2 dataset

Classifier	Method					Measures							
	CT		ST			Sen (%)	Spec (%)	Prec (%)	F1 M (%)	AUC	Acc (%)	FPR	Time (sec)
Trees	✓					77	75	77.3	77.15	0.85	77.1	0.117	16.80
			✓			78.75	76.5	78.0	78.37	0.86	78.1	0.11	4.29
DA	LDA		QDA			Measures							
	✓					98.15	98.3	98.1	98.13	0.98	98.2	0.01	15.64
			✓			91.67	98.5	92.7	92.18	0.96	91.7	0.04	4.04
SVM	LSVM	CSVM	QSVM	MGSVM		Measures							
	✓					97.67	97.5	97.7	97.68	0.99	97.9	0.01	7.29
		✓				91.70	98.5	92.7	92.2	0.97	91.8	0.05	9.16
			✓			97.3	98.5	97.3	97.3	0.99	97.4	0.02	5.30
				✓		90.67	92.0	90.7	90.68	0.96	90.6	0.467	5.21
KNN	FKNN	MKNN	Cosine	Cubic	WKNN	Measures							
	✓					96.5	99	97.0	96.75	0.98	97.4	0.013	4.882
		✓				94.75	98.5	96.0	95.37	0.99	95.8	0.023	4.04
			✓			94.0	97.0	95.0	94.49	0.99	94.8	0.267	4.19
				✓		93.5	99	95.7	94.59	0.99	95.3	0.023	5.97
					✓	97.4	99.0	97.3	97.35	0.99	97.4	0.02	4.02
NN	**MLP**					**98.25**	**98.5**	**98.3**	**98.27**	**1.0**	**98.4**	**0.01**	**3.25**
EBT	Baggage tree					90.67	92.0	91.3	90.98	0.97	91.1	0.043	10.03

*The bold results of Neural Network show the best accuracy

The fusion process includes few drawbacks such as the addition of irrelevant features, redundancy among features, and few more. These kinds of problems make the recognition process complex and time-consuming [55]. Few evolutionary algorithms are reported in state of art using GA and PSO. However, these techniques are time-consuming to optimize fitness function. Compared to these techniques, the physics approaches like entropy methods are fast and efficient on a large number of datasets. In this work, we implemented a CcE approach to select the best features. Mathematically, the CcE technique is represented in Eq. 11.

Let we have fused feature vector (FV) denoted by δF of dimension $N \times 2048$, where, N denotes the number of samples that are used for training and testing process and 2048 denotes the length of fused features. We used K-Means clustering on fused FV with k = 2. As, we defined the clusters $\{C_k, k = 1, 2\}$. Then, the posterior probability of the defined clusters is computed as follows:

$$P(C_k|\delta F) = P(\delta F|C_k)P(C_k)|P(\delta F) \propto P(\delta F|C_k)P(C_k) \quad (11)$$

The cost function of K-Means clustering is defined as follows:

$$\sum_{\lambda_i \in C_k} \left[(\psi_i - C_k)^2 / 2\sigma^2 \right] + (\delta F) \quad (12)$$

After that, we computed the entropy of each cluster and selected the highest value features through weights posterior probability assignment. The entropy function of this work is modified as:

$$P(\delta F|C_k) = exp\left(W \sum_{\lambda_i \in C_k} \ln\left(P\left(\psi_i | C_k \right) \right) \right) \quad (13)$$

Where, ψ_i denotes the expected outcome features, W is a weight parameter which is formulated as $W = \frac{C_k}{n}$.

Finally, top features are selected according to the values that are higher than W. The selected features are finally classified through neural network (NN) [4]. The performance of these results is compared with several other classification algorithms like SVM, KNN, and few more [10–12]. The sample results of the proposed workflow are shown in Fig. 8.

Table 5 Verification for classification results of the neural network in the form of CM

Cancer type	Cancer type		
	Common	Melanoma	Benign
Common	**100%**		
Melanoma		**98%**	2%
Benign		3%	**97%**

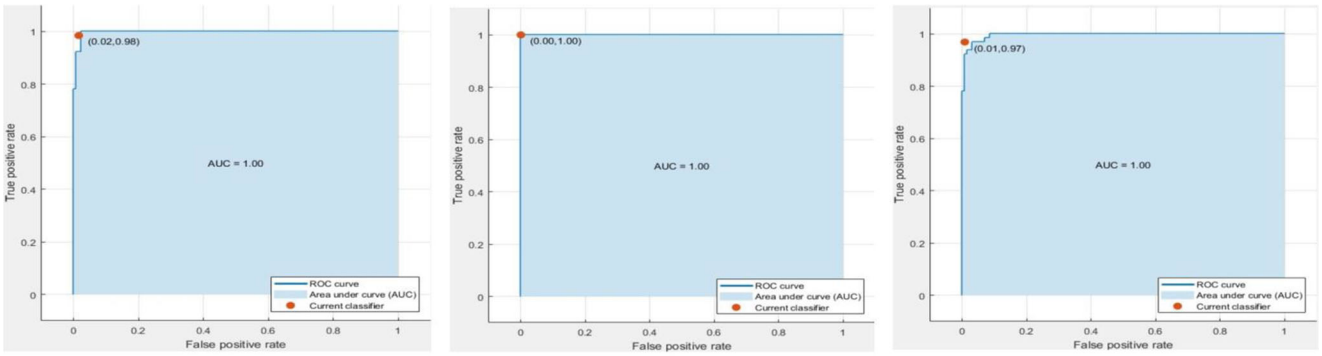

Melanoma Common Nevi Benign

Fig. 10 Presentation of PH2 dataset results in the form of ROC curves

Experimental results and discussion

Experimental Setup

The proposed skin lesion identification and recognition system are evaluated on three publically dermoscopic datasets including PH2, and ISBI series (2016 and 2017). The experimental results are obtained in two steps. In the first step, lesion identification is performed through the proposed contrast-enhanced CNN along with the thresholding. The experiments are achieved on PH2 and ISIC 2017 datasets. In the second phase, the best-selected features are classified through different types of classifiers such as decision trees (DT), discriminant analysis (LDA), support vector machine (SVM), k-nearest neighbor (KNN), ensemble methods, and neural network (NN). We utilized neural network in this work for its best results and compared its performance with other state-of-the-art classifiers. The classifiers mentioned above are utilized in the classification phase. They also include a few advanced techniques like simple trees, fine trees, cubic SVM, weighted KNN, ensemble subspace discriminant analysis (ESDA), and few more as defined in the results section. The analysis of NN is performed on the selected datasets through 8 performance metrics like sensitivity (sen), specificity (spec), precision

Table 6 Proposed recognition results through HD based features fusion and CcE selection approach using ISBI 2016 dataset

Classifier	Method					Measures							
	CT		ST			Sen (%)	Spec (%)	Prec (%)	F1 M (%)	AUC	Acc (%)	FPR	Time (sec)
Trees	✓					90.5	90	90.5	90.5	0.93	90.8	0.095	13.68
			✓			91.5	94	92.0	91.69	0.91	91.8	0.085	9.34
Discriminant	LDA		QDA			Measures							
	✓					88.5	83	89	88.75	0.92	88.5	0.115	9.58
			✓			88.0	91.5	91.5	89.72	0.94	91.4	0.085	8.39
Support Vector Machine	LSVM	CSVM	QSVM	MGSVM	CGSVM	Measures							
	✓					94.0	91.0	94.0	94	0.98	93.8	0.06	9.84
		✓				92.5	93.0	92.5	92.5	0.97	92.4	0.15	8.70
			✓			91.5	92.0	92.0	91.75	0.98	91.8	0.08	8.75
				✓		92.0	90.0	92.5	92.25	0.97	92.1	0.08	8.50
					✓	89.0	83.0	89.5	89.25	0.96	88.8	0.11	8.37
K-Nearest Neighbor	FKNN	MKNN	Cosine	Cubic	W-KNN	Measures							
	✓					86.0	90.0	90.5	88.20	0.90	89.8	0.10	8.59
		✓				87.5	78.0	89.5	88.5	0.96	87.8	0.125	8.03
			✓			86.0	90.5	91.0	88.42	0.97	90.8	0.095	8.59
				✓		89.5	83.0	90.0	89.75	0.96	89.5	0.105	10.67
					✓	89.0	81.0	90.5	89.75	0.96	89.1	0.105	7.97
Neural Network	**MLP**					**95.0**	**95.0**	**95.0**	**95.0**	**0.98**	**95.1**	**0.05**	**6.97**
EBT	Baggage tree					92.0	91.0	92.5	92.25	0.97	92.1	0.08	20.59

*The bold results of Neural Network show the best accuracy

Table 7 Verification for classification results of the neural network in the form of CM

Cancer type	Cancer type	
	Benign	Malignant
Benign	**95%**	5%
Malignant	5%	**95%**

(pre), F1-measure (F1-M), AUC, false positive rate (FPR), accuracy (Acc), and recognition execution time. All experiments are performed on MATLAB using Desktop Computer Corei7 with 16GB of RAM and 8GB graphic card.

Datasets

In this work, we utilized three famous dermoscopy (DY) datasets; ISBI 2016, ISBI 2017, and PH2. The PH2 dataset consists of a total of 200 8-bit DY images of resolution 768 × 660. The total of 200 DY images includes 80 benign, 80 common nevi, and 40 melanoma. In addition, the ground truth images of all 200 DY images are also provided by expert doctors and publically available for the segmentation process [56].

The ISBI 2016 challenge includes a total of 1279 DY images. This challenge includes separate tasks such as segmentation, features detection, and classification of lesions into the relevant category. For the training process, 900 images are utilized from total DY samples and 379 images for the testing process [57].

The ISBI 2017 challenge includes the total of 2750 DY RGB images of resolution 296-1456. From the total, 2233 images are benign, and 517 are melanoma. For the experimental evaluation, 2000 images are utilized for the training process and the remaining 750 for testing the proposed system [58]. The few of sample images are shown in Fig. 9.

Segmentation results

The two well-known performance metrics: accuracy and negative rate (NR) are calculated for performance analysis of lesion segmentation. The ISIC 2017 and PH2 datasets are utilized in this regards. The annotated images of both datasets are provided by experts and are publically available. The total 2000 images of ISIC 2017 dataset is utilized, and a few best results (30 images) are given in Table 1. The overall average accuracy achieved for all 2000 images is 94.98%. The overall error rate is 5.22 which is less (almost 1%) as compared to the latest state of the art techniques.

Similarly, the segmentation results of PH2 dataset are also given in Table 2. The total of 200 DY samples experiments; however, results are exhibited on few images. The overall average accuracy of all 200 images is 95.41% and the error rate is 4.59% which is less (almost 0.52%) as compared to the latest techniques.

The comparison of the proposed segmentation results with the latest techniques is conducted in Table 3. The recent maximum achieved accuracy of ISIC 2017 dataset is 94.08% [56]. Whereas, our method shows improvement in accuracy up to 0.7% and reached 94.78% for ISIC 2017 dataset. Similarly, for PH2 dataset, the previous best-reported accuracy is 95.30% [56] and our method reached 95.41% accuracy which shows 0.11% improvement.

Recognition results

In the lesion recognition task, three datasets are utilized for the system analysis. The extracted CNN features are fused and

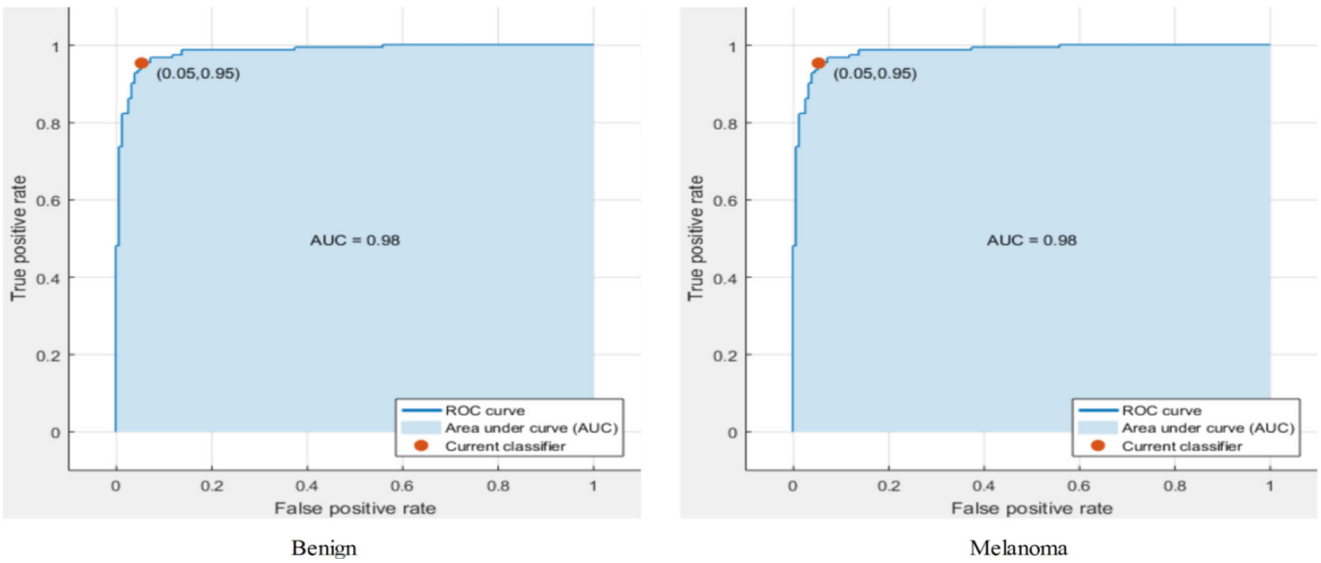

Fig. 11 Presentation of ISBI 2016 dataset results in the form of ROC curves

Table 8 Proposed recognition results through HD based features fusion and CcE selection approach using ISBI 2017 dataset

*Meth	Method					Measures							
	CT	ST				Sen (%)	Spec (%)	Prec (%)	F1 M (%)	AUC	Acc (%)	FPR	Time (sec)
Trees	✓					91.5	93	91.5	91.5	0.95	91.7	0.085	8.87
		✓				88.5	85	89	88.75	0.91	88.7	0.115	12.15
DA	LDA	QDA				Measures							
	✓					94	95	94	94	0.94	94.3	0.06	12.4
		✓				93.3	99.1	93.1	93.45	0.96	93.4	0.08	24.96
SVM	L SVM	C SVM	Q-SVM	MG-SVM	CG-SVM	Measures							
	✓					94	99	94.5	94.25	0.97	94.1	0.06	10.9
		✓				85.5	87	85.5	85.5	0.92	85.6	0.14	139.43
			✓			94	99	94.5	94.25	0.98	94.0	0.06	22.52
				✓		94	98	94	94	0.98	94.0	0.06	15.64
					✓	93	99	93.5	93.25	0.97	93.0	0.07	14.59
KNN	FKNN	M-KNN	Cosine	Cubic	W KNN	Measures							
	✓					92.5	94	92.5	92.5	0.92	92.5	0.07	10.68
		✓				94	100	94.5	94.25	0.97	93.8	0.06	9.898
			✓			94	99	94.5	94.25	0.98	94.1	0.05	10.89
				✓		93	99	93.5	93.25	0.97	93.1	0.07	99.94
					✓	99	100	94.5	96.7	0.97	94.1	0.06	14.81
NN	**MLP**					**94.5**	**98**	**95**	**94.75**	**0.98**	**94.8**	**0.05**	**10.91**
EBT	Baggage tree					94	99	94.5	94.25	0.98	94.0	0.06	22.52

*The bold results of Neural Network show the best accuracy. *Meth denotes method or classifiers

best subset of features is selected through CcE based approach. Later, the selected best features are classified using NN and few other state-of-the-art algorithms for comparison purpose. In addition, the advanced methods of these classifiers such as complex tree and simple tree are used for DT. Similarly, for discriminant analysis, the LDA and QDA are employed, for SVM, LSVM, CSVM, QSVM, and MGSVM are implemented. A 70:30 approach is utilized to divide the datasets into training and testing procedures. Then, k-fold cross validation is performed where k = 20 which normally selected as k = 10, but we selected this value for more reliable and consistent results.

The recognition performance of PH2 dataset in terms of a different number of classifiers and their performance matrices are presented in Table 4. In this Table, the best-achieved accuracy is 98.4% for NN, whereas the other parameters such as Sen, Spec, Pre, F1-M, AUC, and FPR are 98.25%, 98.5%, 8.3%, 98.27%, 1.0%, and 0.01, respectively. The best accuracy values of the other classifiers such as DT, DA, SVM, KNN, and EBT are 78.1%, 98.2% 97.9%, 97.4%, and 91.1% using ST, LDA, LSVM, W-KNN, and baggage trees, respectively. The recognition accuracy of NN is also verified through a confusion matrix (CM) and ROC curves as presented in Table 5 and Fig. 10. In addition, the execution time of the recognition process is computed for all classifiers and the top three best recorded times are 3.25 s, 4.02 s, and 4.04 s for NN, weighted KNN, medium KNN, respectively.

Table 9 Verification for classification results of the neural network in the form of CM

Cancer type	Cancer type	
	Benign	Malignant
Benign	**98%**	2%
Malignant	9%	**91%**

The recognition accuracy values of ISBI 2016 dataset for all the selected classifiers are presented in Table 6. The best-noted accuracy is 95.1% using NN through MLP method. The other achieved measures like Sen, Spec, Prec, F1-M, AUC, and FPR are 95.0%, 95.0%, 95.0%, 95%, 0.98, and 0.05, respectively. The other classifiers such as DT, DA, SVM, KNN, and EBT achieved the best accuracy of 91.8%, 91.4%, 93.8%, 90.8%, and 92.1% using ST, QDA, LSVM, cosine-KNN, and baggage trees, respectively. The recognition accuracy of NN using MLP method is also verified through a confusion matrix (CM) and ROC curves as presented in Table 7 and Fig. 11. In addition, the execution time of the recognition process is also computed for all the selected classification

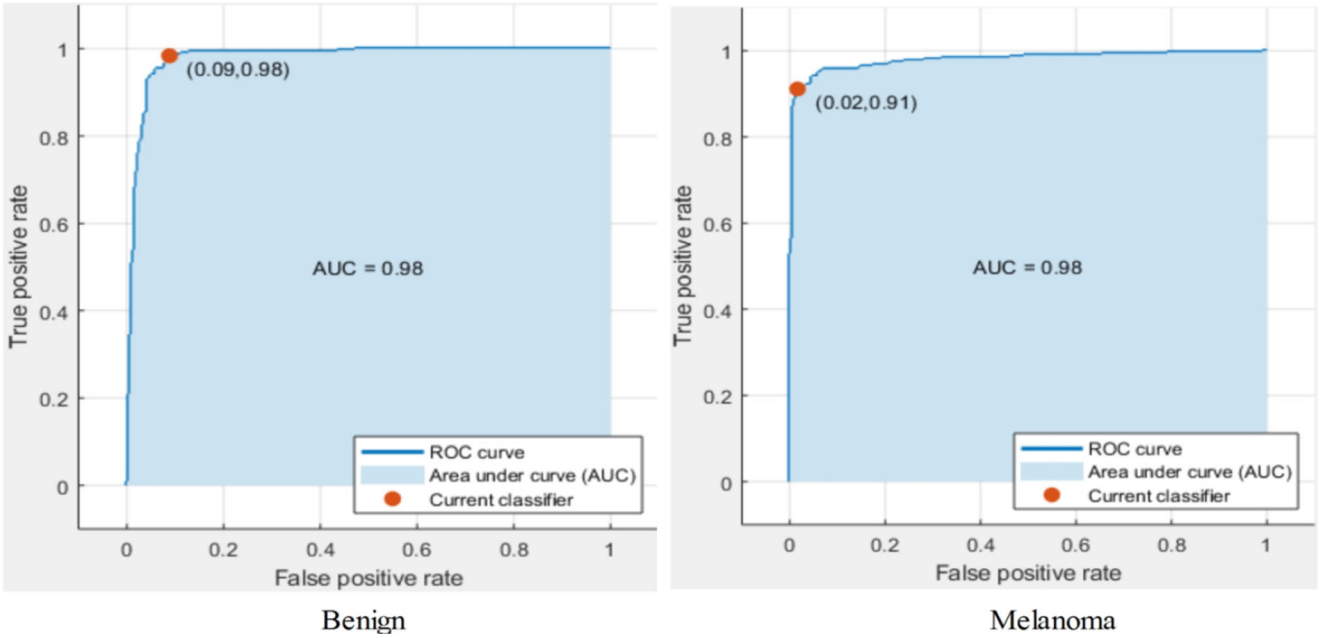

Fig. 12 Presentation of ISBI 2017 dataset results in the form of ROC curves

methods, and the best recorded time is 6.97 s. The other two best execution performances are 7.97 and 8.03 s for W-KNN and MKNN methods, respectively.

In Table 8, the detailed recognition results are presented for ISBI 2017 dataset. Similar to the PH2 and ISBI 2016 datasets evaluation process, the same classifiers and performance measures are employed for this dataset. The best-recorded accuracy is 94.8% which is obtained through NN. The other calculated measures like Sen, Spec, Prec, F1-M, AUC, and FPR are 94.5%, 98%, 95%, 94.75%, 0.98, and 0.055%, respectively. The best accuracy values of DT, DA, SVM, KNN, and EBT are 91.7%, 94.3%, 94.1%, 94.1%, and 94%, respectively using CT, LDA, LSVM, weighted KNN, and baggage tree methods, respectively. In Table 9, the CM is given which is used for verification of the proposed accuracy using NN. In addition, the confirmation of NN achievement is also shown through ROC curves in Fig. 12. The comparison of the running time is also carried out for all the selected classifiers in Table 9 using the proposed method. The best reported computational time is 8.876 for decision trees (DT) method like a complex tree (CT).

Comparison and Analysis

In this section, the analysis of the proposed approach is conducted in terms of both numerical values and visual results like enhancement, lesion boundary extraction, and labeled images. The overall architecture of the proposed system is shown

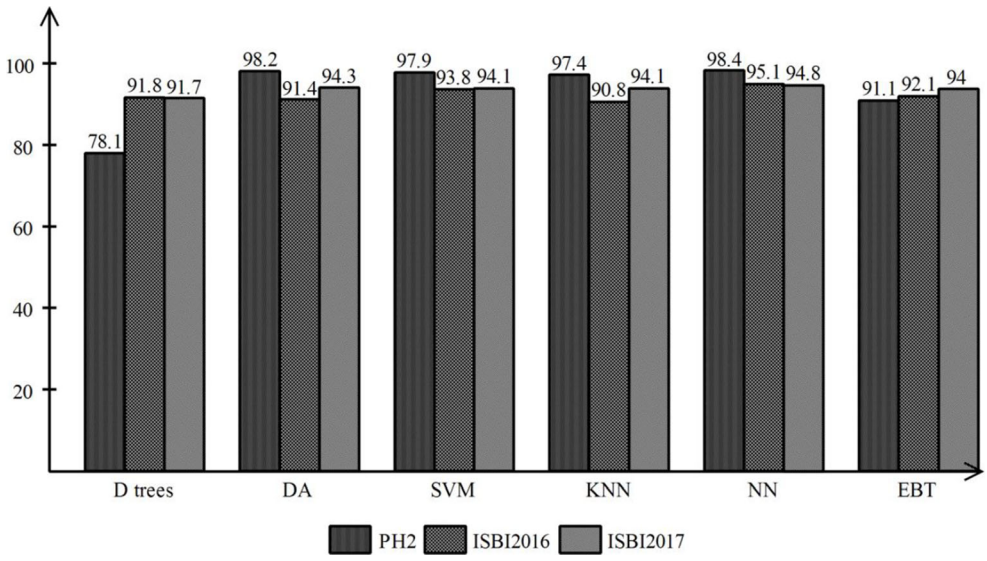

Fig. 13 Graphical comparison of best accuracies of each classification method for all three selected datasets

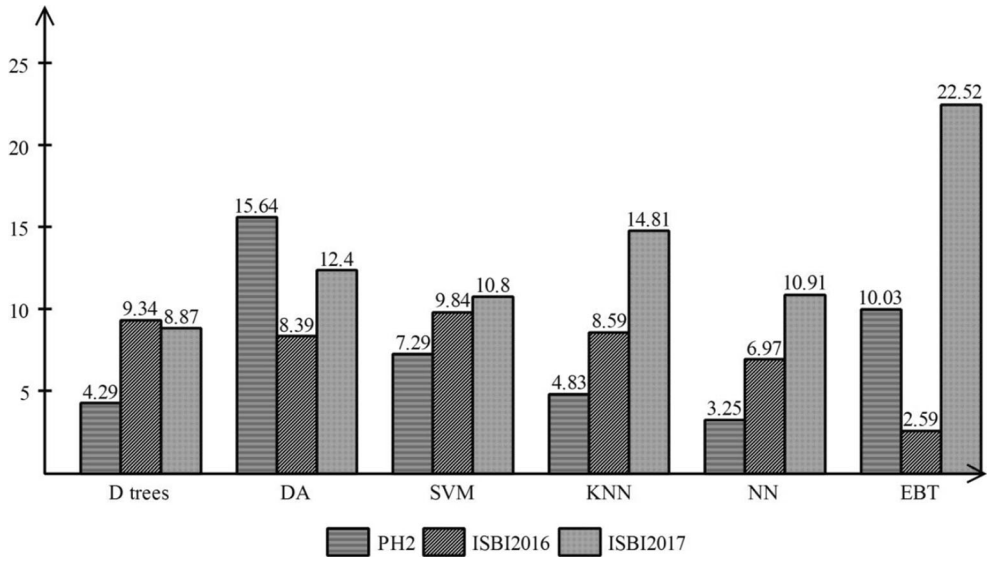

Fig. 14 Graphical representation of classification time which are listed in Fig. 13 for all datasets

in Fig. 1 whereas the visual enhancement and DCNN based segmentation effects are shown in Figs. 2, 3, 4, and 5. The proposed segmentation method is validated on ISIC 2017 and PH2 datasets and the obtained results are presented in Tables 1 and 2. In the recognition phase, the CNN features are extracted and fused through HD based approach and the visual effects are shown in Fig. 7. The overall labeled recognition results are shown in Fig. 8. The recognition process is validated on ISBI 2016, ISBI 2017, and PH2 datasets and the obtained results are presented in Tables 3-9 and their ROC's are displayed in Figs. 10-12. In Fig. 13, a comparison of each classification method for all three selected datasets is presented which shows the superiority of NN compared to the other techniques. In addition, the classification time is also plotted in Fig. 14. From Fig. 14, NN performed efficiently compared to the other methods.

Table 10 Comparison with existing techniques for all selected datasets

Method	Year	Dataset	Accuracy (%)
[4]	2018	PH2	97.5
[64]	2017	PH2	96.0
[65]	2018	PH2	97.5
[26]	2017	PH2	97.0
Proposed	2019	PH2	98.4
[4]	2018	ISBI 2016	83.2
[66]	2018	ISBI 2016	86.1
[8]	2017	ISBI 2016	94.9
Proposed	2019	ISBI 2016	95.1
[4]	2018	ISBI 2017	88.2
[67]	2018	ISBI 2017	93.6
[68]	2017	ISBI 2017	93.4
Proposed	2019	ISBI 2017	94.8

The proposed method is also compared with the latest techniques using the three selected datasets in term of accuracy as addressed in Table 10. In [4], the authors presented the handcrafted features and the entropy-based selection approach for lesion classification. They reached an accuracy of 97.5% using PH2 dataset. Waheed et al. [64] presented an efficient machine learning approach for skin lesion classification and reported an accuracy of 96% using PH2 dataset. Similarly in [26, 69], the authors introduced the hand-crafted and the deep CNN based methods for lesion classification and achieved an accuracy of 97.5% and 97%, respectively. The proposed method achieves an accuracy of 98.4% on PH2 dataset. Like PH2 dataset, the comparison is also conducted for ISBI 2016 and 2017 datasets with the latest approaches ([68]; M Attique [4, 8, 66, 67]). Recently, Yu et al. [8] achieved an accuracy of 94.9% using ISBI 2016 dataset, whereas our method achieves an accuracy of 95.1%. In [68], Bi et al. reported an accuracy of 93.4% which is later improved by [67] with more than 0.2%. The proposed method achieves an accuracy of 94.8% for ISBI 2017 dataset which gives the validity of the proposed deep learning method.

Conclusion

In this article, we proposed a new fully automated enhanced deep CNN model for skin lesion border identification and lesion recognition. The proposed heterogeneous framework includes three major pipeline procedures including augmentation and contrast enhancement, color pixels based on CNN training and segmentation, and CNN features fusion and selection. The best subset of selected features is classified through NN. A comparison result is conducted for each dataset using several classification methods. The segmentation results are evaluated on PH2 and ISIC 2017 datasets

and attained an average accuracy of 95.41% and 94.78%, respectively. The proposed recognition process is evaluated on ISIB 2016, 17, and PH2 datasets and attained the best accuracy of 95.1%, 94.8%, and 98.4%, respectively. The proposed system accuracy is better as compared to the existing state-of-the-art segmentation and recognition techniques which shows the authenticity of our method. Moreover, from the obtained results, we conclude that the selection of the most relevant pixels of lesion regions provides good segmentation results that later affect the recognition process. We also notice that the selection of the best subset of features reduces the overall system execution time. In the future, we shall attain only the segmentation process using transferring learning and physics selection theorems. Through physics selection theorems, the best subsets of features are selected.

Acknowledgements This work was supported by the research Project [Skin Cancer Melanoma Detection from Dermoscopic Images Using Machine Learning Techniques]; Prince Sultan University; Saudi Arabia [SSP -18-5-04]Additionally, in part supported by Artificial Intelligence and Data Analytics (AIDA) Lab Prince Sultan University Riyadh Saudi Arabia. Authors are thankful for the support.

This work was supported by the Research Project (SSP -18-5-04). Additionally, in part supported by Artificial Intelligence and Data Analytics (AIDA) Lab Prince Sultan University Riyadh Saudi Arabia. Authors are thankful for the support.

References

1. Rogers, H. W., Weinstock, M. A., Feldman, S. R., and Coldiron, B. M., Incidence estimate of nonmelanoma skin cancer (keratinocyte carcinomas) in the US population, 2012. JAMA Dermatology 151(10):1081–1086, 2015.
2. Jerant, A. F., Johnson, J. T., Demastes Sheridan, C., and Caffrey, T. J., Early detection and treatment of skin cancer. American family physician 62(2), 2000.
3. Balch, C. M., Gershenwald, J. E., Soong, S.-J., Thompson, J. F., Atkins, M. B., Byrd, D. R. et al., Final version of 2009 AJCC melanoma staging and classification. Journal of clinical oncology 27(36):6199, 2009.
4. Khan, M. A., Akram, T., Sharif, M., Awais, M., Javed, K., Ali, H., and Saba, T., CCDF: Automatic system for segmentation and recognition of fruit crops diseases based on correlation coefficient and deep CNN features. Computers and Electronics in Agriculture 155: 220–236, 2018.
5. Nasir, M., Khan, M. A., Sharif, M., Lali, I. U., Saba, T., Iqbal, T., An improved strategy for skin lesion detection and classification using uniform segmentation and feature selection based approach, Microscopy research and technique 81(6):528–543, 2018. https://doi.org/10.1002/jemt.23009
6. Binder, M., Schwarz, M., Winkler, A., Steiner, A., Kaider, A., Wolff, K., and Pehamberger, H., Epiluminescence microscopy: a useful tool for the diagnosis of pigmented skin lesions for formally trained dermatologists. Archives of Dermatology 131(3):286–291, 1995.
7. Abbas, Q., Garcia, I., and Rashid, M., Automatic skin tumor border detection for digital dermoscopy using a new digital image analysis scheme. British Journal of Biomedical Science 67(4):177–183, 2010.
8. Yu, L., Chen, H., Dou, Q., Qin, J., and Heng, P.-A., Automated melanoma recognition in dermoscopy images via very deep residual networks. IEEE Transactions on Medical Imaging 36(4):994–1004, 2017.
9. Korotkov, K., and Garcia, R., Computerized analysis of pigmented skin lesions: a review. Artificial Intelligence in Medicine 56(2):69–90, 2012.
10. Khan, M. A., Akram, T., Sharif, M., Saba, T., Javed, K., Lali, I. U. et al., Construction of saliency map and hybrid set of features for efficient segmentation and classification of skin lesion. Microsc Res Tech, 2019a. https://doi.org/10.1002/jemt.23220.
11. Khan, S. A., Nazir, M., Khan, M. A., Saba, T., Javed, K., Rehman, A., Akram, T., and Awais, M., Lungs nodule detection framework from computed tomography images using support vector machine. Microsc Res Tech., 2019b. https://doi.org/10.1002/jemt.23275.
12. Khan, M. A., Lali, I. U., Rehman, A., Ishaq, M., Sharif, M., Saba, T., Zahoor, S., and Akram, T., Brain tumor detection and classification: A framework of marker-based watershed algorithm and multilevel priority features selection. Microscopy Research and Technique, 2019c. https://doi.org/10.1002/jemt.23238.
13. Yousaf, K., Mehmood, Z., Saba, T., Rehman, A., Munshi, A. M., Alharbey, R., and Rashid, M., Mobile-health applications for the efficient delivery of health care facility to people with dementia (PwD) and support to their carers: A survey. BioMed Research International 2019:1–26, 2019.
14. Suzuki, K., Overview of deep learning in medical imaging. Radiological Physics and Technology 10(3):257–273, 2017.
15. Shen, D., Wu, G., and Suk, H.-I., Deep learning in medical image analysis. Annual Review of Biomedical Engineering 19:221–248, 2017.
16. Ching, T., Himmelstein, D. S., Beaulieu-Jones, B. K., Kalinin, A. A., Do, B. T., Way, G. P. et al., Opportunities and obstacles for deep learning in biology and medicine. Journal of The Royal Society Interface 15(141):20170387, 2018.
17. Norouzi, A., Rahim, M. S. M., Altameem, A., Saba, T., Rada, A. E., Rehman, A., and Uddin, M., Medical image segmentation methods, algorithms, and applications. IETE Technical Review 31(3):199–213, 2014. https://doi.org/10.1080/02564602.2014.906861.
18. Lee, T., Ng, V., Gallagher, R., Coldman, A., and McLean, D., Dullrazor®: A software approach to hair removal from images. Computers in Biology and Medicine 27(6):533–543, 1997.
19. Kiani, K., and Sharafat, A. R., E-shaver: An improved DullRazor® for digitally removing dark and light-colored hairs in dermoscopic images. Computers in Biology and Medicine 41(3):139–145, 2011.
20. Liu, Z., and Zerubia, J., Skin image illumination modeling and chromophore identification for melanoma diagnosis. Physics in Medicine & Biology 60(9):3415, 2015.
21. Emre Celebi, M., Kingravi, H. A., Iyatomi, H., Alp Aslandogan, Y., Stoecker, W. V., Moss, R. H. et al., Border detection in dermoscopy images using statistical region merging. Skin Research and Technology 14(3):347–353, 2008.
22. Gómez, D. D., Butakoff, C., Ersboll, B. K., and Stoecker, W., Independent histogram pursuit for segmentation of skin lesions. IEEE Transactions on Biomedical Engineering 55(1):157–161, 2008.
23. Silveira, M., Nascimento, J. C., Marques, J. S., Marçal, A. R., Mendonça, T., Yamauchi, S. et al., Comparison of segmentation methods for melanoma diagnosis in dermoscopy images. IEEE Journal of Selected Topics in Signal Processing 3(1):35–45, 2009.
24. Yao, Q., Guan, Z., Zhou, Y., Tang, J., Hu, Y., & Yang, B. (2009). *Application of support vector machine for detecting rice diseases using shape and color texture features*. Paper presented at the Engineering Computation, 2009. ICEC'09. International Conference on.

25. Sadeghi, M., Lee, T. K., McLean, D. I., Lui, H., and Atkins, M. S., Detection and analysis of irregular streaks in dermoscopic images of skin lesions. IEEE Trans. Med. Imaging 32(5):849–861, 2013.
26. Satheesha, T., Satyanarayana, D., Prasad, M. G., and Dhruve, K. D., Melanoma is Skin Deep: A 3D reconstruction technique for computerized dermoscopic skin lesion classification. IEEE Journal of Translational Engineering in Health and Medicine 5:1–17, 2017.
27. Celebi, M. E., and Zornberg, A., Automated quantification of clinically significant colors in dermoscopy images and its application to skin lesion classification. IEEE systems journal 8(3):980–984, 2014.
28. Tschandl, P., Sinz, C., and Kittler, H., Domain-specific classification-pretrained fully convolutional network encoders for skin lesion segmentation. Computers in biology and medicine 104:111–116, 2019.
29. Mahbod, A., Schaefer, G., Ellinger, I., Ecker, R., Pitiot, A., and Wang, C., Fusing fine-tuned deep features for skin lesion classification. Computerized Medical Imaging and Graphics 71:19–29, 2019.
30. Rebouças Filho, P. P., Peixoto, S. A., da Nóbrega, R. V. M., Hemanth, D. J., Medeiros, A. G., Sangaiah, A. K., and de Albuquerque, V. H. C., Automatic histologically-closer classification of skin lesions. Computerized Medical Imaging and Graphics., 2018.
31. Oliveira, R. B., Papa, J. P., Pereira, A. S., and Tavares, J. M. R., Computational methods for pigmented skin lesion classification in images: review and future trends. Neural Computing and Applications 29(3):613–636, 2018.
32. Ray, S. (2018). Disease Classification within Dermascopic Images Using features extracted by ResNet50 and classification through Deep Forest. *arXiv preprint arXiv:1807.05711*.
33. Eaton-Rosen, Z., Bragman, F., Ourselin, S., & Cardoso, M. J. (2018). Improving Data Augmentation for Medical Image Segmentation.
34. Paris, S., Hasinoff, S. W., and Kautz, J., Local Laplacian filters: Edge-aware image processing with a Laplacian pyramid. ACM Trans. Graph. 30(4):61–68, 2011 12.
35. Kaur, R., Stoecker, W. V. D., Mishra, N. K., & Kasmi, R. (2018). Thresholding methods for lesion segmentation in dermoscopy images: Google Patents.
36. Guo, Y., Ashour, A. S., and Smarandache, F., A Novel Skin Lesion Detection Approach Using Neutrosophic Clustering and Adaptive Region Growing in Dermoscopy Images. Symmetry 10(4):119, 2018.
37. Xu, H., & Hwang, T. H. (2018). Automatic Skin Lesion Segmentation Using Deep Fully Convolutional Networks. *arXiv preprint arXiv:1807.06466*.
38. Jamal, A., Hazim Alkawaz, M., Rehman, A., and Saba, T., (2017) Retinal imaging analysis based on vessel detection. Microsc Res Tech. 80(17):799–811, 2017. https://doi.org/10.1002/jemt.
39. Rahim, M. S. M., Rehman, A., Kurniawan, F., and Saba, T., Ear biometrics for human classification based on region features mining. Biomedical Research, vol. 28(10):4660–4664, 2017.
40. Duan, Q., Akram, T., Duan, P., & Wang, X., Visual saliency detection using information contents weighting. Optik 127(19):7418–7430, 2016.
41. Mughal, B., Muhammad, N., Sharif, M., Rehman, A., and Saba, T., Removal of pectoral muscle based on topographic map and shape-shifting silhouette. BMC Cancer, 2018. https://doi.org/10.1186/s12885-018-4638-5.
42. Mughal, B., Muhammad, N., Sharif, M., Saba, T., and Rehman, A., Extraction of breast border and removal of pectoral muscle in wavelet, domain. Biomedical Research 28(11):5041–5043, 2017a.
43. Mughal, B., Sharif, M., Muhammad, N., and Saba, T., A novel classification scheme to decline the mortality rate among women due to breast tumor. Microscopy Research and Technique, 2017b. https://doi.org/10.1002/jemt.22961.
44. Saba, T., Khan, S. U., Islam, N., Abbas, N., Rehman, A. et al., Cloud-based decision support system for the detection and classification of malignant cells in breast cancer using breast cytology images. Microscopy Research and Technique, 2019. https://doi.org/10.1002/jemt.23222.
45. Saba, T., Al-Zahrani, S., and Rehman, A., Expert system for offline clinical guidelines and treatment. Life Sci Journal 9(4):2639–2658, 2012.
46. Iqbal, S., Khan, M. U. G., Saba, T., Mehmood, Z., Javaid, N., Rehman, A., and Abbasi, R., Deep learning model integrating features and novel classifiers fusion for brain tumor segmentation. Microscopy Research and Technique, 2019. https://doi.org/10.1002/jemt.23281.
47. Saba, T., Rehman, A., Mehmood, Z., Kolivand, H., and Sharif, M., Image Enhancement and Segmentation Techniques for Detection of Knee Joint Diseases: A Survey. Current Medical Imaging Reviews 14(5), 2018b. https://doi.org/10.2174/1573405613666170912164546.
48. Saba, T., Bokhari, S. T. F., Sharif, M., Yasmin, M., and Raza, M., Fundus image classification methods for the detection of glaucoma: A review. Microsc Res Tech., 2018a. https://doi.org/10.1002/jemt.23094.
49. Sadad, T., Munir, A., Saba, T., and Hussain, A., Fuzzy C-means and region growing based classification of tumor from mammograms using hybrid texture feature. Journal of Computational Science 29:34–45, 2018.
50. Ullah, H., Saba, T., Islam, N., Abbas, N., Rehman, A., Mehmood, Z., Anjum, A., An ensemble classification of exudates in color fundus images using an evolutionary algorithm based optimal features selection, Microscopy research and technique, 2019. https://doi.org/10.1002/jemt.23178.
51. Iqbal, S., Ghani, M. U., Saba, T., and Rehman, A., Brain tumor segmentation in multi-spectral MRI using convolutional neural networks (CNN). Microsc Res Tech. 81(4):419–427, 2018. https://doi.org/10.1002/jemt.22994.
52. Iqbal, S., Khan, M. U. G., Saba, T., and Rehman, A., Computer assisted brain tumor type discrimination using magnetic resonance imaging features. Biomedical Engineering Letters 8(1):5–28, 2017. https://doi.org/10.1007/s13534-017-0050-3.
53. Tahir, B. Iqbal, S., Khan, M.U.G., Saba, T., Mehmood, Z., Anjum, A., Mahmood, T. (2019) Feature enhancement framework for brain tumor segmentation and classification, https://doi.org/10.1002/jemt.23224.
54. Szegedy, C., Vanhoucke, V., Ioffe, S., Shlens, J., & Wojna, Z. (2016). *Rethinking the inception architecture for computer vision.* Paper presented at the Proceedings of the IEEE conference on computer vision and pattern recognition.
55. Sharif, M., Khan, M. A., Akram, T., Javed, M. Y., Saba, T., and Rehman, A., A framework of human detection and action recognition based on uniform segmentation and combination of Euclidean distance and joint entropy-based features selection. EURASIP Journal on Image and Video Processing 2017(1):89, 2017.
56. Bi, L., Kim, J., Ahn, E., Kumar, A., Feng, D., and Fulham, M., Step-wise integration of deep class-specific learning for dermoscopic image segmentation. Pattern recognition 85:78–89, 2019.
57. Wu, J. T., Dernoncourt, F., Gehrmann, S., Tyler, P. D., Moseley, E. T., Carlson, E. T. et al., Behind the scenes: A medical natural language processing project. International Journal of Medical Informatics 112:68–73, 2018.
58. Codella, N. C., Gutman, D., Celebi, M. E., Helba, B., Marchetti, M. A., Dusza, S. W., … Kittler, H. (2018). *Skin lesion analysis toward melanoma detection: A challenge at the 2017 international symposium on biomedical imaging (ISBI), hosted by the international skin*

imaging collaboration (ISIC). Paper presented at the Biomedical Imaging (ISBI 2018), 2018 IEEE 15th International Symposium on.
59. Navarro, F., Escudero-Vinolo, M., and Bescos, J., Accurate segmentation and registration of skin lesion images to evaluate lesion change. IEEE Journal of Biomedical and Health Informatics, 2018.
60. Li, Y., and Shen, L., Skin lesion analysis towards melanoma detection using deep learning network. Sensors 18(2):556, 2018.
61. Soudani, A., and Barhoumi, W., An image-based segmentation recommender using crowdsourcing and transfer learning for skin lesion extraction. Expert Systems with Applications 118:400–410, 2019.
62. Gutiérrez-Arriola, J. M., Gómez-Álvarez, M., Osma-Ruiz, V., Sáenz-Lechón, N., & Fraile, R. (2017). Skin lesion segmentation based on preprocessing, thresholding and neural networks. *arXiv preprint arXiv:1703.04845*.
63. Bi, L., Kim, J., Ahn, E., Kumar, A., Fulham, M., and Feng, D., Dermoscopic image segmentation via multi-stage fully convolutional networks. IEEE Trans. Biomed. Eng 64(9):2065–2074, 2017a.
64. Waheed, Z., Waheed, A., Zafar, M., & Riaz, F. (2017). *An efficient machine learning approach for the detection of melanoma using dermoscopic images.* Paper presented at the Communication, Computing and Digital Systems (C-CODE), International Conference on.
65. Akram, T., Khan, M. A., Sharif, M., & Yasmin, M., Skin lesion segmentation and recognition using multichannel saliency estimation and MSVM on selected serially fused features. Journal of Ambient Intelligence and Humanized Computing, 1–20, 2018.
66. Sultana, N. N., Mandal, B., and Puhan, N., Deep residual network with regularised fisher framework for detection of melanoma. IET Computer Vision 12(8):1096–1104, 2018.
67. Sarker, M., Kamal, M., Rashwan, H. A., Banu, S. F., Saleh, A., Singh, V. K., … Radeva, P. (2018). SLSDeep: Skin Lesion Segmentation Based on Dilated Residual and Pyramid Pooling Networks. *arXiv preprint arXiv:1805.10241*.
68. Bi, L., Kim, J., Ahn, E., & Feng, D. (2017b). Automatic skin lesion analysis using large-scale dermoscopy images and deep residual networks. *arXiv preprint arXiv:1703.04197*.
69. Afza, F., Khan, M. A., Sharif, M., and Rehman, A., Microscopic skin laceration segmentation and classification: A framework of statistical normal distribution and optimal feature selection. Microscopy Research and Technique., 2019. https://doi.org/10.1002/jemt.23301.